



Article

# A Tuning Fork Gyroscope with a Polygon-Shaped Vibration Beam

Qiang Xu, Zhanqiang Hou \*, Yunbin Kuang, Tongqiao Miao, Fenlan Ou, Ming Zhuo, Dingbang Xiao and Xuezhong Wu \*

College of Intelligence Science and Engineering, National University of Defense Technology, Changsha 410073, China; xuqiang09@nudt.edu.cn (Q.X.); kuangyunbin16@nudt.edu.cn (Y.K.); miaotongqiao16@nudt.edu.cn (T.M.); oufenlan15@nudt.edu.cn (F.O.); zhuoming@nudt.edu.cn (M.Z.); dingbangxiao@nudt.edu.cn (D.X.)

\* Correspondence: houzhanqiang@nudt.edu.cn (Z.H.); xzwu@nudt.edu.cn (X.W.)

Received: 22 October 2019; Accepted: 18 November 2019; Published: 25 November 2019



**Abstract:** In this paper, a tuning fork gyroscope with a polygon-shaped vibration beam is proposed. The vibration structure of the gyroscope consists of a polygon-shaped vibration beam, two supporting beams, and four vibration masts. The spindle azimuth of the vibration beam is critical for performance improvement. As the spindle azimuth increases, the proposed vibration structure generates more driving amplitude and reduces the initial capacitance gap, so as to improve the signal-to-noise ratio (SNR) of the gyroscope. However, after taking the driving amplitude and the driving voltage into consideration comprehensively, the optimized spindle azimuth of the vibration beam is designed in an appropriate range. Then, both wet etching and dry etching processes are applied to its manufacture. After that, the fabricated gyroscope is packaged in a vacuum ceramic tube after bonding. Combining automatic gain control and weak capacitance detection technology, the closed-loop control circuit of the drive mode is implemented, and high precision output circuit is achieved for the gyroscope. Finally, the proposed Micro Electro Mechanical Systems (MEMS) gyroscope system demonstrates a bias instability of  $0.589^\circ/\text{h}$ , an angular random walk (ARW) of  $0.038^\circ/\sqrt{\text{h}}$ , and a bandwidth of greater than 100 Hz in a full scale range of  $\pm 200^\circ/\text{s}$  at room temperature.

**Keywords:** tuning fork gyroscope; spindle azimuth; vibration beam; bias instability; angular random walk

## 1. Introduction

The Micro Electro Mechanical Systems (MEMS) gyroscope has had great importance in all countries over the past 20 years due to its small size, low cost, low power consumption, and batch fabrication. Micromachined gyroscopes have been widely used in the fields of electronics consumer goods, vehicle safety, weaponry, and other fields [1–3]. A significant amount of research has been carried out on the different kinds of micromachined gyroscopes over the past decades, which has directly promoted the development of high performance gyroscopes for various applications. Among the different kinds of MEMS gyroscopes, the typical structures include turning forks (TFG) [4–8], combs [9–11], rings or disks [12–15], or micro wineglass [16–18].

The most common type of MEMS gyroscope design is the TFG, a shuttling proof mass design that can be operated in either mode-matched or mode-split conditions. Matched mode tuning fork gyroscopes achieved near navigation-grade performance in [19], where values of  $0.003^\circ/\sqrt{\text{h}}$  angular random walk (ARW) and  $0.16^\circ/\text{h}$  bias instability were reported. However, its bandwidth was only 1 Hz, failing most navigation application requirements (usually larger than 100 Hz). On the contrary, a gyroscope working in split mode will have a wider bandwidth, but the mechanical sensitivity is not high. So far, there is no split mode gyroscope that can be compared with the performance of a

mode-matched gyroscope. In summary, split mode tuning fork micromachined gyroscopes that can meet the requirements of inertial level are rarely reported.

Therefore, enhancing the sensitivity is important for split mode tuning fork gyroscopes. The application field for gyroscopes is determined by their sensitivity; only those gyroscopes with high sensitivity can be applied in the fields requiring small variation in angular velocity. Additionally, the signal-to-noise ratio (SNR) of the gyroscope system will increase after the sensitivity is improved. When the same intensity signal is output by the system, the overall noise of the system is relatively reduced.

It is known that greater driving amplitude and larger initial capacities can lead to higher SNR as well as sensitivity. However, if the driving amplitude is too large, the vertical component displacements will be so great that the vibration mass will collide with the glass substrate. Therefore, the gap between the vibration structure and glass (initial capacitive gap) must be larger to avoid the collision. However, this larger gap could result in low sensitivity due to the smaller initial capacity. Therefore, the vertical component of driving displacement becomes one of key factors limiting the sensitivity of tuning fork gyroscopes. In order to reduce the restriction, the vertical component of the driving displacement must be decreased. However, the vertical component of the driving displacement is related to the spindle azimuth of the vibration beam. Therefore, reasonable design of the cross-section of the vibration beam could improve the spindle azimuth, so as to enhance the sensitivity of the tuning fork gyroscope.

The vibration beam of the micromachined tuning fork gyroscope in our research group is a parallelogram beam, which is fabricated by wet etching [20,21]. Driven by the vertical driving force, the vibration structure generates both horizontal and vertical displacements caused by the parallelogram vibration beam. As there is no structure with a high aspect ratio, this kind of gyroscope structure can be fabricated only by anisotropic wet etching process on a single crystal silicon chip, without advanced dry etching process equipment [22,23]. The processing technology is simple and the cost is low due to the low price of the materials used. However, the spindle azimuth of the parallelogram beam is no larger than  $54.74^\circ$ . Therefore, the sensitivity of the gyroscope is low due to the small spindle azimuth being limited by wet etching process.

A novel silicon bulk gyroscope was proposed by the Sensoror company [24–26]. The overall size of the gyroscope structure is very small, benefiting from the unique processing technology, which combines the dry and wet etching. The cross-section of the vibration beam is an irregular polygon, whose spindle azimuth was designed by changing the processing parameters, so the sensitivity of the gyroscope was enhanced by increasing the spindle azimuth. However, as for the dry etching process, it has a strong dependence on advanced processing equipment, and small structure processing requires Silicon-On-Insulator (SOI) chips, which makes the fabrication process more complex and costly than for single crystal silicon chips.

A vibration beam adopting a polygonal cross-section was proposed in order to enhance sensitivity and robustness [27]. Comparison between the proposed polygonal vibration beam and the convex vibration beam on the tolerance capacity analysis was carried out. After comparison, the conclusion was made that the polygonal oblique beam had better tolerance for fabrication imperfections than the convex oblique beam.

Taking all the different kinds of MEMS gyroscopes mentioned above into consideration, in this paper, a tuning fork gyroscope with a polygon-shaped vibration beam is presented. Based on a single crystal silicon chip, the structure is manufactured using processing technology that combines dry and wet etching. Therefore, the following benefits can be obtained:

1. The spindle azimuth can be increased by designing the cross-section of the vibration beam. Therefore, the proposed structure with the optimized vibration beam not only increases the driving amplitude, but also reduces the initial capacitance gap in the sensing direction, so as to enhance the signal-to-noise ratio (SNR) as well as the sensitivity of the gyroscope.

2. The polygonal vibration beam fabricated by the wet and dry etching is much more stable and much more insensitive to the fabrication imperfections, which provides the tuning fork gyroscope with good robustness and repeatability.
3. The use of single crystal silicon chips instead of SOI chips reduces the complexity and cost of the fabrication process.

## 2. Materials and Methods Design for the Proposed Gyroscope

The main idea of the design of the vibration structure is to optimize the cross-section of the vibration beam by improving the spindle azimuth, which should reduce the vertical driving amplitude and enlarge the driving amplitude, so as to enhance the SNR and sensitivity of the gyroscope.

### 2.1. Overall Design of the Proposed Gyroscope

The conventional tuning fork micromachined gyroscope in our work is manufactured by wet etching, and the cross-section of the vibration beam is a parallelogram whose spindle azimuth ( $\theta_p$ ) is no larger than  $54.74^\circ$ , as shown in Figure 1.

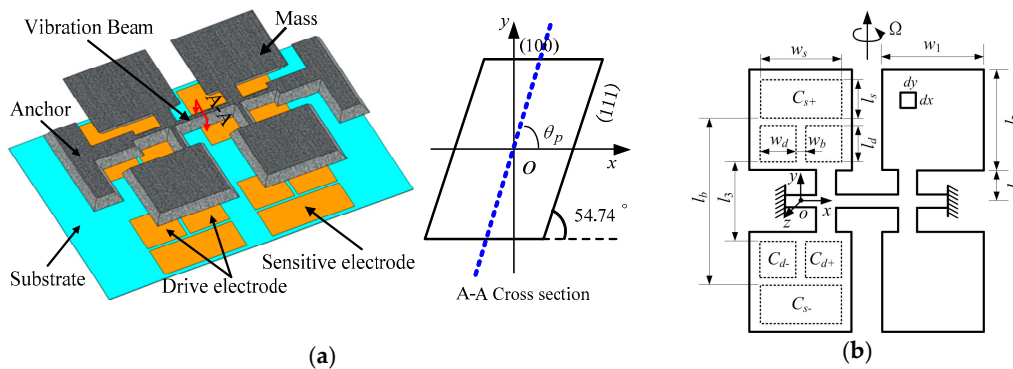


**Figure 1.** Conventional tuning fork micromachined gyroscope. (a) The structure model. (b) The structural parameters.

Here,  $O$  is the rotation center of the driving mode,  $w_d$  is the width of driving electrode,  $w_b$  is the distance between two driving electrodes,  $l_1$  is distance between vibration beam and vibration mass, and  $l_2$  is the length of the vibration mass.

When excited in the driving mode, the vibration mass can generate both horizontal and vertical displacements, as shown in Figure 2. *DriveX* is the horizontal component of driving displacement, *DriveZ* is the vertical component of driving displacement, and  $d$  is the initial capacitance gap ( $d$ ).

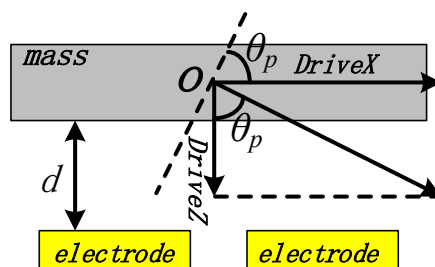


**Figure 2.** Vertical and horizontal component of driving displacement.

According to Figure 2, *DriveX* and *DriveZ* can be described as:

$$\begin{cases} DriveX = \phi_d \cdot \sin(\theta_p) \cdot (l_1 + l_2) / 2 \\ DriveZ = \phi_d \cdot \cos(\theta_p) \cdot (w_d + w_b) / 2 \end{cases} \quad (1)$$

The maximum vertical component of driving displacement ( $MaxdriveZ$ ) is  $d/3$ , due to the pull-in effect. Therefore, the maximum horizontal component of the driving displacement ( $MaxdriveX$ ) can be described as:

$$MaxdriveX = (d/3) \cdot \tan(\theta_p) \cdot (l_1 + l_2) / (w_d + w_b) \tag{2}$$

From Equation (2), we can see that if the other parameters are constant,  $MaxdriveX$  will become larger as the  $\theta_p$  grows larger.

In order to enlarge the driving amplitude and enhance the SNR, the cross-section of the vibration beam is designed to increase the spindle azimuth. The proposed structure is fabricated by both wet and dry etching, as shown in Figure 3. The cross-section is an irregular polygon whose spindle azimuth could be designed by changing processing parameters.

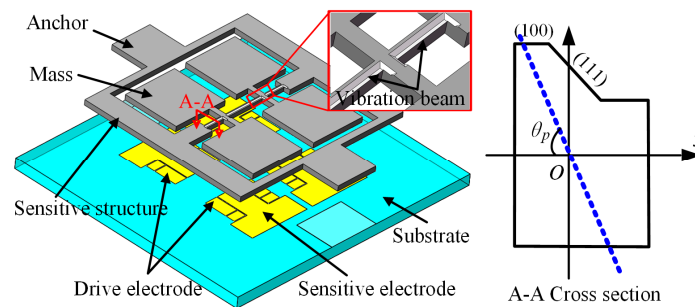


Figure 3. Proposed gyroscope with optimized vibration beam.

### 2.2. Impact Factors of the Spindle Azimuth

The spindle azimuth of the vibration beam is related to the driving amplitude, and it can be increased by optimizing the cross-section shape of the vibration beam.

According to Equation (2), the  $MaxdriveX$  is plotted under different gaps ( $d$ ). As can be seen in Figure 4, the  $MaxdriveX$  grows with the increase of  $\theta_p$  and gap ( $d$ ). The closer  $\theta_p$  is to  $90^\circ$ , the faster the  $MaxdriveX$  increases, especially when  $\theta_p$  is greater than  $80^\circ$ . Therefore, in order to improve the driving amplitude and enhance the SNR, a larger  $\theta_p$  should be chosen in the following design.

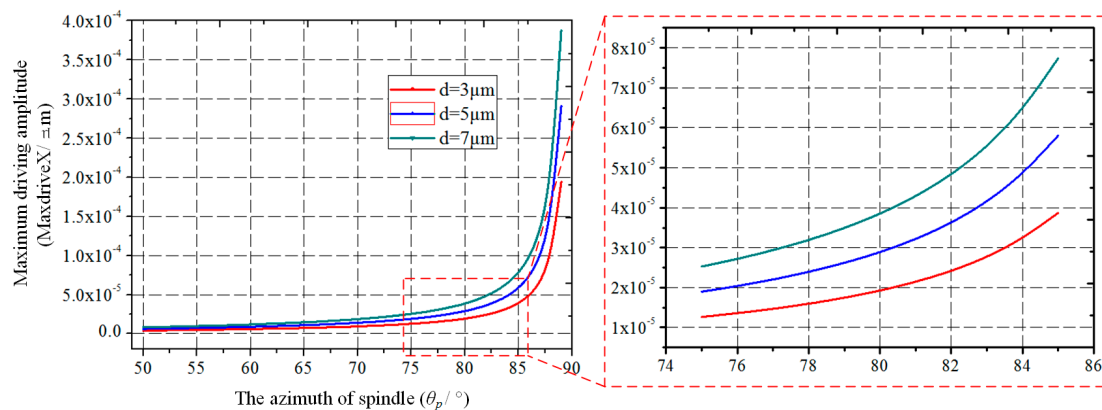


Figure 4. The maximum horizontal component of the driving displacement ( $MaxdriveX$ ) varies with the spindle azimuth ( $\theta_p$ ) and initial capacitance gap ( $d$ ).

As the spindle azimuth ( $\theta_p$ ) and initial gap ( $d$ ) grow, the  $MaxdriveX$  will be enhanced. However, the driving voltage required to drive the vibration mass will be much higher, resulting from the mechanical characteristics of vibration beams with a large spindle azimuth.

According to the research our previous research, the AC voltage ( $V_{ac}$ ), which is required to drive the vibration mass to  $d/3$  in the vertical displacement, can be described as [27]:

$$V_{ac} = \frac{I_d \omega_d^2 d^3}{3\epsilon l_y X_d A_d V_{dc} Q_d} \sec^2(\theta_p) \tag{3}$$

where  $I_d$  is the moment of inertia of the driving axis,  $\omega_d$  is the frequency of the driving mode,  $d$  is the initial capacitor gap between the silicon structure and the glass electrode substrate,  $\epsilon$  is the electric constant,  $l_y$  is the distance from the rotation center to the far end of the mass,  $X_d$  is the half distance of the two adjacent driving capacitor centers,  $A_d$  is the area of the driving electrodes,  $V_{dc}$  is the DC voltage required to drive the structure, and  $Q_d$  is the quality factor of the driving mode.

According to Equation (3), when the other parameters are constant, the relationship between  $V_{ac}$  and  $\theta_p$  is as shown in Figure 5. As can be seen from the curve, when  $\theta_p$  is greater than  $80^\circ$ , the required driving AC voltage ( $V_{ac}$ ) grows quickly, which is difficult when designing a high-voltage circuit.

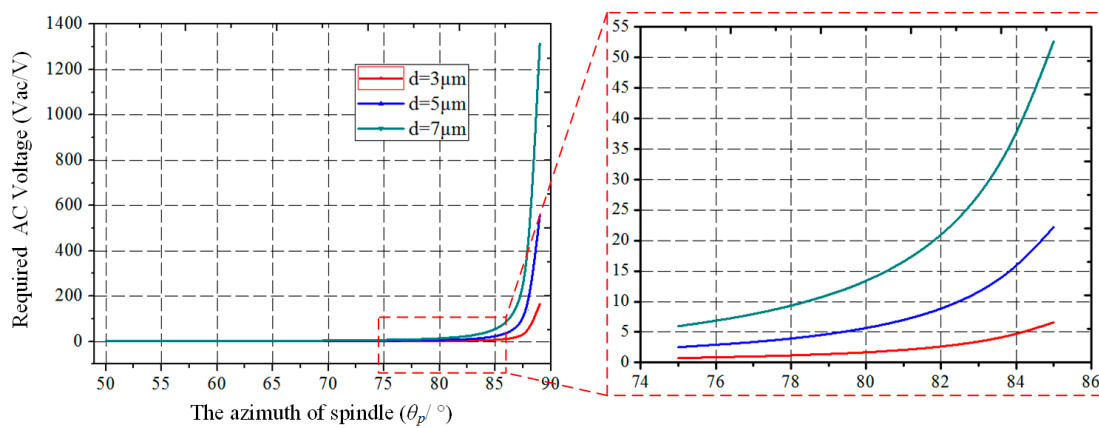


Figure 5. The required AC driving voltage ( $V_{ac}$ ) varies with the spindle azimuth.

In the design of the spindle azimuth ( $\theta_p$ ), both the high sensitivity and low driving voltage should be taken into consideration.

### 2.3. Calculation of the Spindle Azimuth

The key dimensions of the cross-section of the proposed vibration beam are shown in Figure 6.

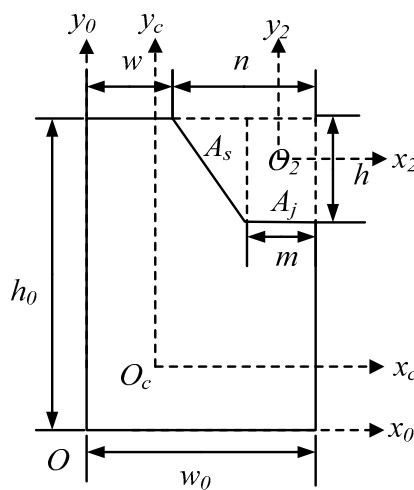


Figure 6. The key dimensions of the cross-section of the proposed vibration beam.

From Figure 6, it can be seen that wet etching is carried out on the basis of a large rectangle, and the right-angled trapezoid part is fabricated by wet etching. Here,  $O_c$  is the centroid of the irregular polygon, and  $O_2$  is the centroid of the right-angle trapezoid, which consists a right triangle ( $A_s$ ) and a small rectangle ( $A_j$ ).

Therefore, the spindle azimuth of the proposed vibration beam can be accurately controlled by changing the width ( $w$ ) and depth ( $h$ ) of wet etching.

In order to design the spindle azimuth of the irregular polygon ( $\theta_p$ ), the moments of inertia ( $I_{x_c}$  and  $I_{y_c}$ ) and the product of inertia ( $I_{x_c y_c}$ ) of the irregular polygon should be calculated beforehand, after which the spindle azimuth can be calculated and described as [28]:

$$angle = angle = 90 - \arctan[2 \cdot I_{x_c y_c} / (I_{y_c} - I_{x_c})] / (2 \cdot \pi \cdot 180) = f(w, h) \quad (4)$$

According to Equation (4), we can see that the spindle azimuth of the irregular polygon ( $\theta_p$ ) is affected by the width ( $w$ ) and depth ( $h$ ) of wet etching, as shown in Figure 7.

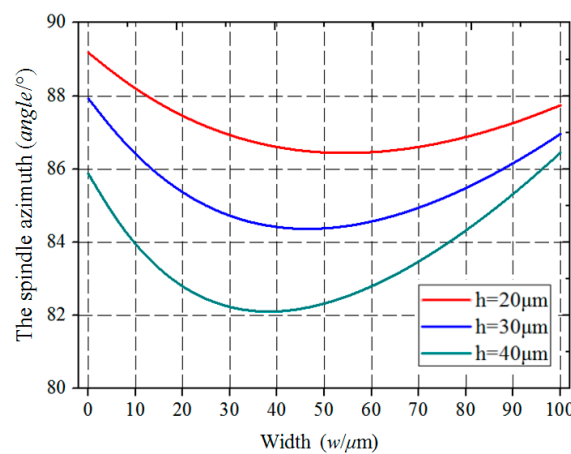


Figure 7. The spindle azimuth ( $\theta_p$ ) varies with the width ( $w$ ) and depth ( $h$ ) of wet etching.

#### 2.4. Design of the Main Dimensions of the Cross-Section

According to Figure 7, when the other conditions are constant, the spindle azimuth ( $\theta_p$ ) decrease as the depth ( $h$ ) of wet etching deepens, and the spindle azimuth ( $\theta_p$ ) decreases first and then increases as the width ( $w$ ) becomes wider. Therefore, when designing the spindle azimuth ( $\theta_p$ ), the zone around the minimum point on the curve is a better choice due to the insensitivity to dimensional errors of width ( $w$ ).

When the width ( $w$ ) becomes larger, the curves with different etching depths ( $h$ ) become closer. That is to say, the spindle azimuth ( $\theta_p$ ) is insensitive to dimensional errors of wet etching depth ( $h$ ) when the width of wet etching ( $w$ ) becomes larger.

In order to obtain a better spindle azimuth ( $\theta_p$ ) that is less affected by fabrication errors, both the width error and depth error should be considered comprehensively. The different processing parameters for the spindle azimuth are calculated with the same processing errors.

After comparison between the different approaches, the optimized combination of structure parameters is obtained, providing insensitivity to dimensional errors. As can be seen in Figure 8, point A is the ideal design of the spindle azimuth on the second line, and the other four points (B, C, D, and E) are the results with 1 μm error in depth and 2 μm error in width.

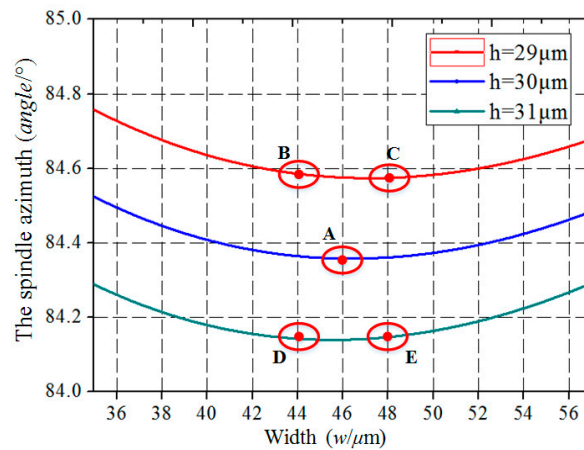


Figure 8. The spindle azimuth ( $\theta_p$ ) varies with the processing errors.

The optimized structural parameters of the proposed vibration structure are determined by theoretical analysis, finite element simulation, and experimental verification. Using the finite element analysis method, the modal simulation analysis of the tuning fork gyroscope is carried out in the simulation software COMSOL Multiphysics, and the simulation motion form of the working mode of the gyroscope can be obtained. The simulation results for drive and sense modes are shown in Figure 9.

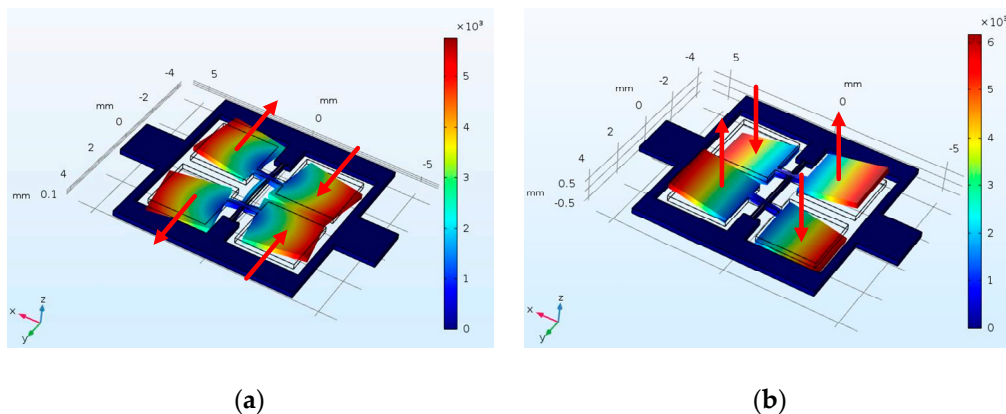


Figure 9. The modal simulation results: (a) drive mode (3253.8 Hz); (b) sense mode (3414.7 Hz).

As can be seen from Figure 9, the drive mode shown in Figure 9a is the bending motion of the vibration beam. The sense mode shown in Figure 9b is the torsional motion of the vibration beam.

### 2.4.1. Driving Mode

There are a pair of differential drive electrodes and a detection electrode under each vibration mass block, as shown in Figure 3. When driving voltages are applied to the differential drive electrode plates, the driving electrostatic force will be generated. When excited by the driving electrostatic force, bending deformation occurs in the vibration beam, so the vibration mass block oscillates in the horizontal direction. However, because the azimuth angle of the vibration beam is less than 90 degrees, the vertical driving motion component is also generated. Therefore, in the driving mode of the gyroscope, the vibration mass block has a three-dimensional vibration motion, which consists of the same reciprocating motion frequency in the horizontal direction and the driving component motion in the vertical direction, as shown in Figure 9a.

### 2.4.2. Detection Mode

When the gyroscope is driven in driving mode and there is angular velocity input on the sensitive axis, a Coriolis force will be generated in the direction of detection, according to the principle of Coriolis force. This Coriolis force will cause torsional deformation of the vibration beam, which will cause the vibration mass block to move up and down in the vertical direction, as shown in Figure 9b.

### 2.4.3. Working Condition

The proposed tuning fork gyroscope uses the frequency mismatch model, and its working frequency is the driving mode frequency. The amplitude–frequency response curves of the working modes of the gyroscope can be obtained by frequency response analysis (FRA). The theoretical amplitude–frequency response curves of the tuning fork gyroscope are shown in Figure 10.

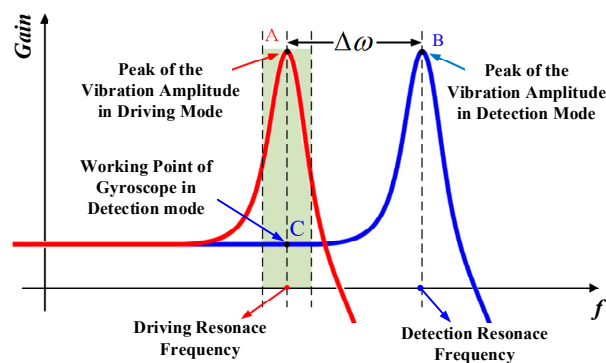


**Figure 10.** The theoretical amplitude–frequency response curves of the tuning fork gyroscope.

As can be seen in Figure 10, points A and B are the peaks of the vibration amplitude in driving and detection curves, respectively. The frequencies of point A and point B are the driving and detection resonance frequencies of the gyroscope. The frequency difference between A and B is defined as the frequency difference of the tuning fork gyroscope. Crossing point C instead of detection resonance frequency point B is the working point of the gyroscope in detection mode. This is why gyroscopes operating in mismatched mode have lower sensitivity but higher stability.

Therefore, in the optimization design of the tuning fork gyroscope, it is necessary to select the operating frequency difference of the gyroscope reasonably. On the premise of ensuring the stability of the working state of the gyroscope, it is of great significance to reduce the frequency difference as much as possible in order to obtain the maximum sensitivity, so as to improve the performance of the gyroscope.

## 3. Fabrication Processing Technology

The fabrication process consists of silicon structure processing, glass electrode substrate processing, bonding processing, and packaging processing.

### 3.1. Fabrication Processing of Silicon Structure and Glass Electrode Substrate

The fabrication processing of the silicon structure, which combines wet and dry etching, can be seen in Figure 11a–f. The fabrication processing of the glass electrode substrate can be seen in Figure 11g–l.



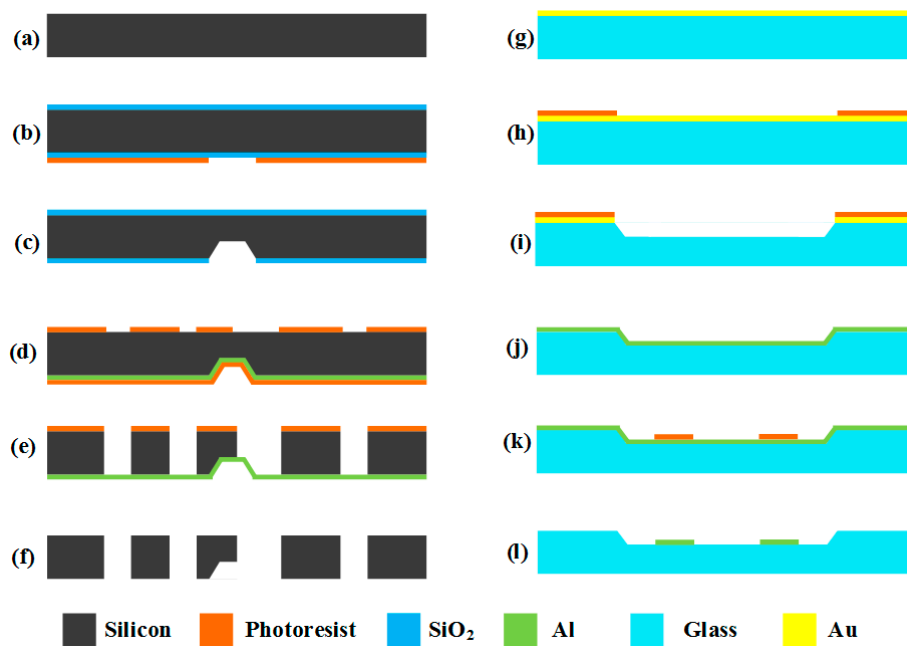


**Figure 11.** Fabrication process of the silicon structure and glass electrode substrate: (a) The processing of the structure starts with a double polished silicon wafer. (b) After high-temperature thermal oxidation, a layer of SiO<sub>2</sub> is grown on the silicon wafer, and then photolithography and development processes are done on the back side of the silicon wafer. Part of the photoresistant layer is removed to prepare for the wet etching in the next step. (c) After removing part of SiO<sub>2</sub>, the remaining SiO<sub>2</sub> is used as a new mask, and then the wet etching process is conducted on the silicon wafer. (d) Firstly, the SiO<sub>2</sub> on both sides is removed, and a layer of aluminum is sputtered on the back side of the silicon wafer as the cut-off layer. Then, a layer of photoresistant layer is used to protect the aluminum from the corrosion of the developer. At last, the second photolithography and development processes are done on the front side of the silicon wafer. Part of photoresistant layer is removed to prepare for the dry etching in the next step. (e) After removing the photoresistant protective layer on the back, dry etching is done on the front side continuously until the whole silicon wafer is etched to the cut-off layer. (f) Removing all of the photoresistant layer and the aluminum, the structure processing is completed. (g) The processing of the electrode substrate starts with a glass wafer, and a layer of gold is evaporated on the front of the glass wafer. (h) The photolithography and development processes are done on the gold layer, and part of photoresistant layer is removed. (i) After removing part of the Au, the remaining Au serves as the mask, and wet etching is done on the glass wafer to make the gaps and provide the motion space for the silicon structure (c). (j,k) After removing all of the photoresistant layer and the Au, a layer of aluminum is sputtered on the gap. Then, the photolithography and development processes are done on the aluminum layer. Part of photoresistant layer is then removed, and the rest of the photoresistant layer serves as the mask to prepare for the next step. (l) After removing the aluminum without mask layer protection, the mask layer is removed and the electrode substrate is finished.

### 3.2. Bonding and Packaging Process

The structure and electrode substrate are bonded together with a narrow capacitive gap, which can increase the electromechanical coupling. After bonding, the gyroscopes are packaged in a ceramic chip carrier in a vacuum environment in order to minimize the Brownian noise floor to achieve better performance. The entire device can be observed under an optical microscope, and some parts of the structure can be observed by scanning electron microscope (SEM), as shown in Figure 12.

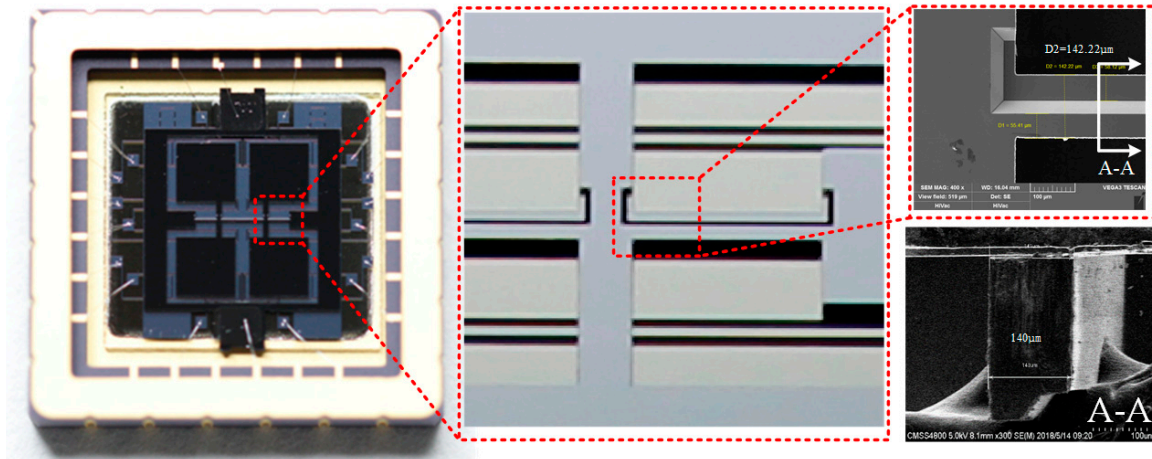


Figure 12. Proposed gyroscopes were packaged in ceramic tubes.

#### 4. Performance Testing

The performance testing of gyroscopes in ceramic tubes mainly includes modal testing and zero bias testing.

##### 4.1. Circuit Signal Processing Technology

There is a detection electrode and a pair of driving electrodes below each vibration mass. When electrodes with the same phase are connected together, the microelectromechanical gyroscope is equivalent to a five-terminal device [29].

As can be seen in Figure 13, the device consists of four capacitors and one common terminal, which is the silicon structure of the gyroscope.  $C_{dt+}$  and  $C_{dt-}$  are the differential capacitances for the driving axis, while  $C_{st+}$  and  $C_{st-}$  are the differential capacitances for the sensing axis. Here,  $V_{d+}$  and  $V_{d-}$  are applied to the driving electrodes, while  $V_{s+}$  and  $V_{s-}$  are applied to the sensing electrodes. (Where, CTV stands for capacitance/voltage converting, HPF stands for high pass filter and LPF stands for low pass filter.)

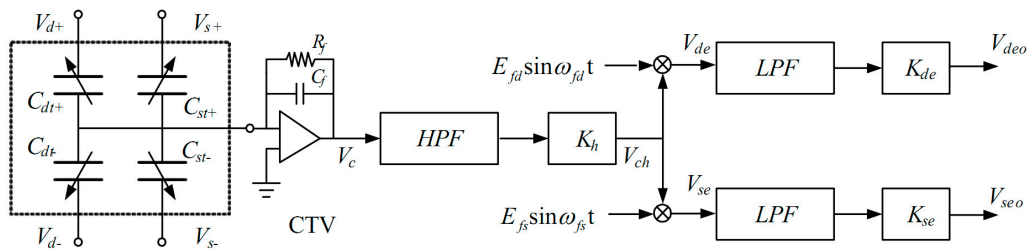


Figure 13. The equivalent model of the gyro circuit.

The voltages applied to the differential capacitance are shown in the following equation:

$$\begin{cases} V_{d+} = V_{dc} + V_{ac} \sin \omega_d t + E_{fd} \sin \omega_{fd} t \\ V_{d-} = V_{dc} - V_{ac} \sin \omega_d t - E_{fd} \sin \omega_{fd} t \\ V_{s+} = E_{fs} \sin \omega_{fs} t \\ V_{s-} = -E_{fs} \sin \omega_{fs} t \end{cases} \quad (5)$$

where  $V_{dc}$  is the DC bias,  $V_{ac} \sin \omega_d t$  is the AC drive voltage,  $E_{fd} \sin \omega_{fd} t$  and  $E_{fs} \sin \omega_{fs} t$  are the high frequency carriers in the driving and sensing axes. All the high frequency carriers come from the

pre-set output of the Microcontroller Unit (MCU). So, the output voltage of the charge amplifier ( $V_c$ ) can be described as:

$$V_c = -(V_{d+}C_{dt+} + V_{d-}C_{dt-} + V_{s+}C_{st+} + V_{s-}C_{st-})/C_f \tag{6}$$

After passing through the high pass filter (HPF) and amplification ( $K_h$ ), the output voltage  $V_{ch}$  can be described as:

$$V_{ch} = -(K_h E_{fd} \sin \omega_{fd} t \Delta C_d) / C_f - (K_h E_{fs} \sin \omega_{fs} t \Delta C_s) / C_f \tag{7}$$

After passing through the multiplier, the signal  $V_{ch}$  is demodulated by the high-frequency driving and sensing carriers, respectively. So, the end output voltages  $V_{deo}$  and  $V_{seo}$  can be described as:

$$\begin{cases} V_{deo} = -(K_h K_{de} E_{fd}^2 \Delta C_d) / 2C_f \\ V_{seo} = -(K_h K_{de} E_{fs}^2 \Delta C_s) / 2C_f \end{cases} \tag{8}$$

From Equation (8), we can see that the output voltages  $V_{deo}$  and  $V_{seo}$  are proportional to the variation of the driving and sensing capacitance, respectively. Thus, the variation of the driving and sensing capacitance can be effectively extracted and separated.

In the closed driving loop, automatic gain control (AGC) technology is used to ensure the stability of the driving voltage. The high frequency carrier signal of the driving voltage is applied to modulate the signal of the high frequency carrier signal. Then, the output signal on the common terminal is demodulated with this carrier signal, and the information for the driving loop can be obtained. The schematic diagram of the closed driving loop control is shown in Figure 14. (Where, C/V stands for capacitance/voltage converting, PID stands for Proportion Integral Differential and REF stands for reference.)

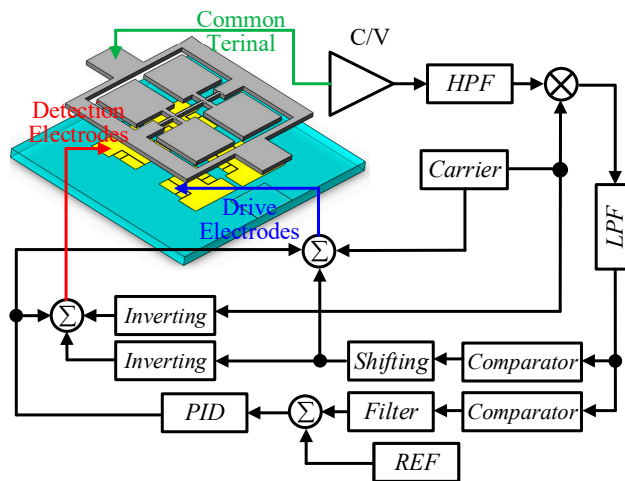


Figure 14. The schematic diagram of the closed driving loop control.

In order to separate the detection loop information from the common terminal and reduce the influence of low-frequency noise, the high-frequency detection carrier is applied to the detection electrodes. The detection capacitance variation signal is modulated to the high frequency of the carrier signal, and the useful signal and the low-frequency noise are successfully separated.

The first demodulation with the high-frequency carrier separates the useful signal from other signals at the common terminal. The frequency of the obtained signal is the frequency of the applied AC driving voltage. The output signal after first demodulation is demodulated by the AC driving voltage for the second time, and the DC voltage signal corresponding to the input angular velocity is obtained, as shown in Figure 15.

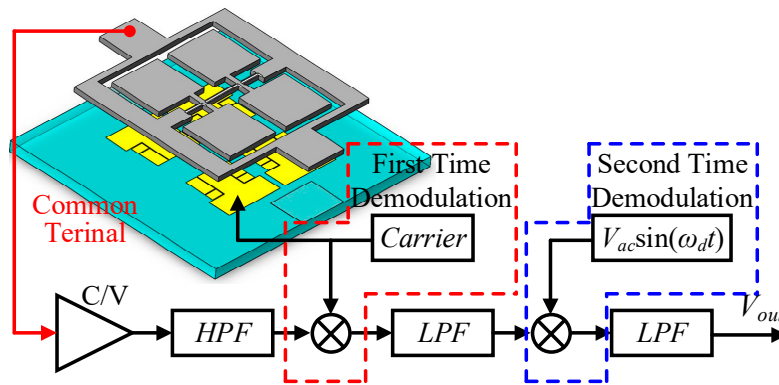


Figure 15. Schematic diagram of weak capacitance detection.

4.2. Modal Testing

Frequency response analysis (FRA) is used to perform modal testing of the proposed gyroscope, and the results are shown in Figure 16. The modal testing is an important part of the performance testing. On the one hand, the natural vibration frequencies of driving and detection modes can be obtained, and the working state of the gyroscope can be accurately detected. On the other hand, the quality factor (Q) of the driving and detection modes can be calculated according to the modal test curves, and the vacuum situation of the gyroscope can be obtained, which provides an important reference for subsequent performance testing.

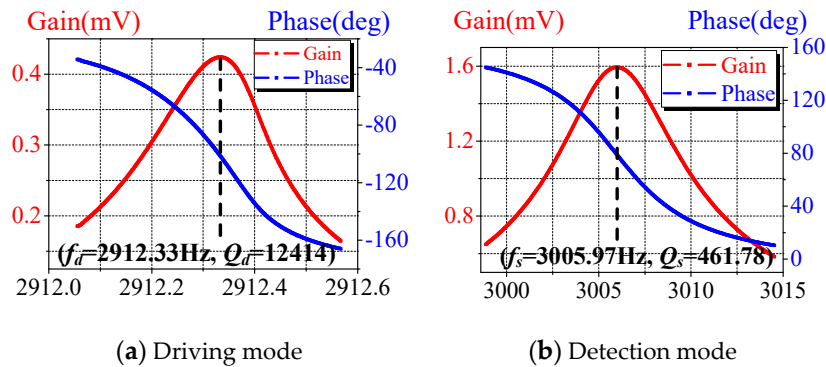


Figure 16. Modal testing of the proposed gyroscope.

According to the characteristics of the micro-gyroscope proposed in this paper, a method combining electrostatic force excitation and capacitance detection is used for modal testing. A frequency response analyzer is used to apply sweep excitation on driving and detection electrodes, and the response of the gyro to the signal is observed. The modal frequencies and Q values are obtained from the frequency response analysis curves. The frequency response analyzer is a FRA5087 from Negative Feedback (NF) company. Its frequency resolution is 0.1 MHz, which meets the test requirements for the gyroscope [30].

The quality factor of the gyroscope is calculated in the  $-3\text{dB}$  bandwidth. The frequency response in the driving direction is shown in Figure 16a, the resonance frequency is 2912.33 Hz, and the quality factor is 12,414. The frequency response in the detection direction is shown in Figure 16b, the resonance frequency is 3005.97 Hz, and the quality factor is 461.78.

4.3. Zero Bias Testing

The zero bias testing is measured at room temperature, and the bias stability of sample reaches about  $1.3^\circ/\text{h}$ , as shown in Figure 17.

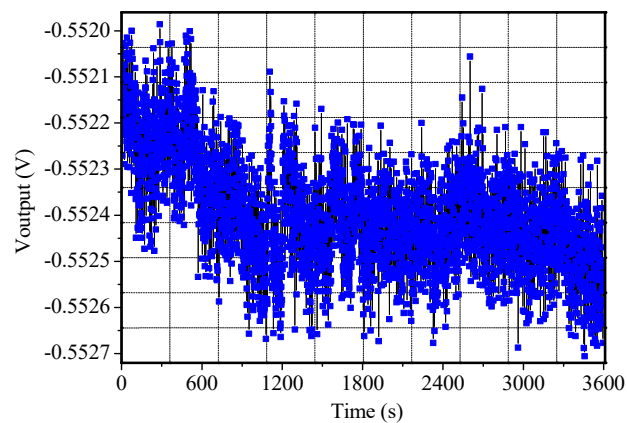


Figure 17. Zero bias output of the sample.

Allan variance is used to analyze the bias stability. The standard definition of bias instability used by inertial sensor manufacturers is the minimum point on the Allan variance curve. The system demonstrates a bias instability of  $0.589^\circ/\text{h}$  and an angular random walk (ARW) of  $0.038^\circ/\sqrt{\text{h}}$ , as shown in Figure 18.

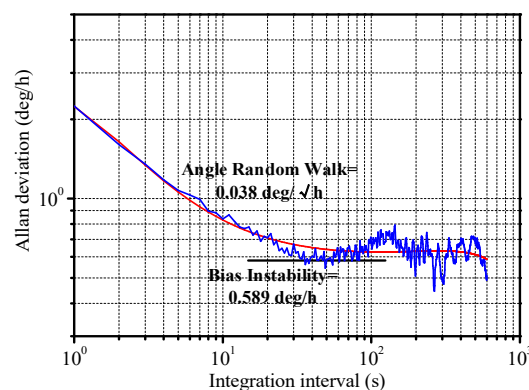


Figure 18. Allan deviation of the sample.

As can be seen from the performance results, compared to other reported high-performance MEMS gyroscope, the performance of the proposed tuning fork gyroscope is not good enough. The noise level of the gyroscope is critical to the performance, and the low noise level of the gyroscope is one of the reasons for its poor performance. So, the analysis of gyroscope noise is carried on, which is helpful for performance improvement.

## 5. Noise Analysis

The resolution and minimum bias stability of the MEMS gyroscope are determined by the noise level of the angular velocity output signal. The noise of the gyroscope system consists of the mechanical thermal noise from the silicon structure and the circuit noise from the detection circuit.

### 5.1. Mechanical Thermal Noise

Mechanical thermal noise is the main noise resource of the MEMS gyroscope. It is caused by irregular thermal motions of gas molecules around inertial mass and molecules inside the structure, and is directly related to the damping of the system. The greater the damping of system, the greater the mechanical thermal noise. The equivalent force of the mechanical thermal noise in the MEMS gyroscope can be described as [31]:

$$F_{mtn} = \sqrt{4k_B T c B} \quad (9)$$

where  $k_B$  is the Boltzmann constant,  $T$  is the absolute temperature in degrees Kelvin,  $c$  is the damping coefficient of the system, and  $B$  is the bandwidth of the gyroscope.

The equivalent angular velocity of the mechanical thermal noise in the gyroscope in this paper can be described as:

$$\Omega_{TMN} = \frac{1}{x_0} \sqrt{\frac{k_b T \omega_s B}{m \omega_d^2 Q_s}} \tag{10}$$

where  $x_0$  is the dynamic displacement along the driving direction,  $\omega_d$  and  $\omega_s$  are the resonant frequencies of driving and detection modes,  $m$  is the equivalent vibration mass, and  $Q_s$  is the quality factor of the detection mode. According to Equation (10), reducing the mechanical thermal noise of the gyroscope so as to improve the performance can be achieved by improving the driving displacement and equivalent vibration mass and increasing the  $Q_s$ .

5.2. Noise in the Detection Circuit

The minimum signal level that a circuit can handle correctly is determined by the noise of the detection circuit. The greater the noise of the circuit, the poorer the ability of the circuit is to detect or process small signals, and the poorer the performance of the gyroscope system. In order to analyze the circuit noise of the gyroscope, the noise model of the gyroscope system needs to be established. The circuit noise of the gyroscope is mainly related to the detection circuit, so the noise analysis in the detection circuit is focused on this. The main noise sources of the gyroscope in the detection circuit can be seen in Figure 19.

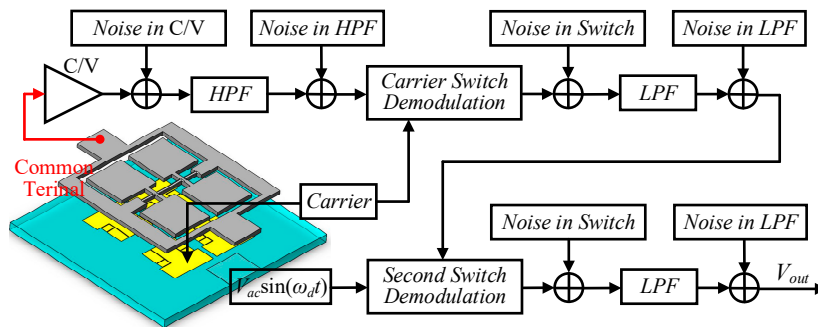


Figure 19. The main noise sources of the gyroscope in detection circuit.

As can be seen in Figure 19, the switch demodulation is conducted at a high frequency, so the noise generated by the switch is restrained after passing through the low pass filter. The charge amplifier is located at the front end of the detection circuit, so the noise generated by the charge amplifier is the main circuit noise.

The noise model of the front-end charge amplifier is established in Figure 20.

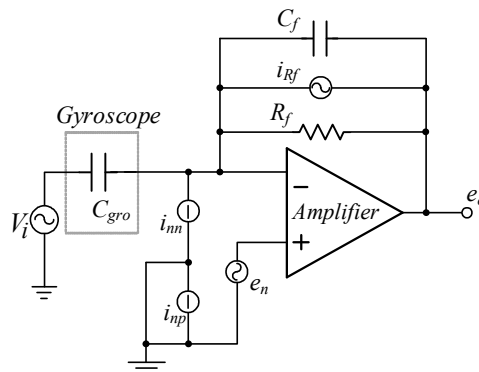


Figure 20. The noise model of the front-end charge amplifier in the detection circuit.

The noise of the front-end charge amplifier mainly includes three parts: equivalent input voltage, circuit noise, and resistance thermal noise. Capacitors do not produce noise, but instead limit the frequency bandwidth of the output voltage. Therefore, the total output noise of the charge amplifier is contributed by the operational amplifier and resistor.

Because of the irrelevance of the noise, the total power density of the output noise can be calculated as:

$$e_{oc}^2 = e_n^2 \left(1 + \frac{C_{gro}}{C_f}\right)^2 + \left(i_{nm}^2 + \frac{4kT}{R_f}\right) \left| \frac{1}{(j\omega C_f)^2} \right|^2 \quad (11)$$

where  $C_{gro}$  is the sum of the driving voltage and detection capacitance of the gyroscope,  $C_f$  is the feedback capacitance of the charge amplifier, and  $R_f$  is the feedback resistor of the charge amplifier.

If  $e_{oc}$  is equivalent to capacitive noise density  $c_{nc}$ , then  $e_{oc}$  can be described as:

$$c_{nc}^2 = e_n^2 \frac{(C_f + C_{gro})^2}{E_{fs}^2} + \left(i_{nm}^2 + \frac{4kT}{R_f}\right) \left| \frac{1}{(j\omega_{fs})^2 E_{fs}^2} \right|^2 \quad (12)$$

According to Equation (12), the main measures to reduce circuit noise are as follows:

- Select a better operational amplifier with lower noise  $e_n$ .
- Increase the frequency of carrier  $\omega_{f2}$ .
- Decrease the feedback capacitor of the charge amplifier  $C_f$ .
- Improve the amplitude of carrier  $E_{f2}$ .

## 6. Conclusions

The design, simulation, fabrication, and experimentation of a novel split-mode, micromachined tuning fork gyroscope has been presented in this paper. Increasing the spindle azimuth of the vibration beam of the gyroscope can not only improve the driving displacement, but can also reduce the vibration gap and enhance the SNR of the sensor. The impact factors of the spindle azimuth of the vibration beam were designed and analyzed. The fabrication processes were demonstrated, including the manufacture of the vibration structure, glass substrate, anodic bonding, and vacuum packaging process. Finally, performance testing of the gyroscope in a ceramic tube was conducted. The zero-rate bias instability and ARW were obtained as 0.589°/h and 0.038°/√h from measurements at room temperature, respectively.

After analyzing the noise of the tuning fork gyroscope, there is still a lot of work to do. On the one hand, it is necessary to improve the processing quality to reduce the mode coupling and zero bias. On the other hand, a better operational amplifier with lower noise should be applied to improve the overall signal-to-noise ratio of the gyroscope and further improve the performance of the gyroscope.

**Author Contributions:** Conceptualization, Z.H. and D.X.; methodology, F.O. and M.Z.; software, Y.K. and T.M.; validation, Q.X. and F.O.; formal analysis, Z.H., D.X., and X.W.; investigation, Q.X. and Z.H.; resources, Z.H., M.Z., and X.W.; data curation, Q.X. and Y.K.; writing—original draft preparation, Q.X.; writing—review and editing, Q.X.; visualization, Z.H. and T.M.; supervision, D.X. and X.W.; project administration, D.X. and X.W.; funding acquisition, D.X. and X.W.

**Funding:** This research received no external funding.

**Acknowledgments:** The authors would like to thank the editors and the reviewers for their help.

**Conflicts of Interest:** The authors declare no conflict of interest.

## References

1. Ma, W.; Lin, Y.; Liu, S.; Zheng, X.; Jin, Z. A novel oscillation control for MEMS vibratory gyroscopes using a modified electromechanical amplitude modulation technique. *J. Micromech. Microeng.* **2016**, *27*, 025005. [[CrossRef](#)]
2. Yang, D.; Woo, J.K.; Lee, S.; Mitchell, J.; Challoner, A.D.; Najafi, K. A micro oven-control system for inertial sensors. *J. Microelectromech. Syst.* **2017**, *26*, 507–518. [[CrossRef](#)]
3. Sung, J.; Kim, J.Y.; Seok, S.; Kwon, H.J.; Kim, M.; Kim, G.; Lim, G. A gyroscope fabrication method for high sensitivity and robustness to fabrication tolerances. *J. Micromech. Microeng.* **2014**, *24*, 075013. [[CrossRef](#)]
4. Nguyen, M.; Ha, N.; Nguyen, L.; Chu, H.; Vu, H. Z-axis micromachined tuning fork gyroscope with low air damping. *Micromachines* **2017**, *8*, 42. [[CrossRef](#)]
5. Yang, C.; Li, H. Digital control system for the MEMS tuning fork gyroscope based on synchronous integral demodulator. *IEEE Sens. J.* **2015**, *15*, 5755–5764. [[CrossRef](#)]
6. Guan, Y.; Gao, S.; Jin, L.; Cao, L. Design and vibration sensitivity of a MEMS tuning fork gyroscope with anchored coupling mechanism. *Microsyst. Technol.* **2016**, *22*, 247–254. [[CrossRef](#)]
7. Zotov, S.A.; Simon, B.R.; Prikhodko, I.P.; Trusov, A.A.; Shkel, A.M. Quality factor maximization through dynamic balancing of tuning fork resonator. *IEEE Sens. J.* **2014**, *14*, 2706–2714. [[CrossRef](#)]
8. Prikhodko, I.P.; Zotov, S.A.; Trusov, A.A.; Shkel, A.M. Foucault pendulum on a chip: Rate integrating silicon MEMS gyroscope. *Sens. Actuat. A-Phys.* **2012**, *177*, 67–78. [[CrossRef](#)]
9. Tatar, E.; Mukherjee, T.; Fedder, G.K. Stress effects and compensation of bias drift in a MEMS vibratory-rate gyroscope. *J. Microelectromech. Syst.* **2017**, *26*, 569–579. [[CrossRef](#)]
10. Park, B.S.; Han, K.; Lee, S.; Yu, M. Analysis of compensation for a g-sensitivity scale-factor error for a MEMS vibratory gyroscope. *J. Micromech. Microeng.* **2015**, *25*, 115006. [[CrossRef](#)]
11. Sonmezoglu, S.; Alper, S.E.; Akin, T. An automatically mode-matched MEMS gyroscope with wide and tunable bandwidth. *J. Microelectromech. Syst.* **2014**, *23*, 284–297. [[CrossRef](#)]
12. Zhou, X.; Xiao, D.; Wu, X.; Wu, Y.; Hou, Z.; He, K.; Li, Q. Stiffness-mass decoupled silicon disk resonator for high resolution gyroscopic application with long decay time constant (8.695 s). *Appl. Phys. Lett.* **2016**, *109*, 263501. [[CrossRef](#)]
13. Behbahani, A.H.; Kim, D.; Stupar, P.; DeNatale, J.; M'Closkey, R.T. Tailored etch profiles for wafer-level frequency tuning of axisymmetric resonators. *J. Microelectromech. Syst.* **2017**, *26*, 333–343. [[CrossRef](#)]
14. Ahn, C.H.; Ng, E.J.; Hong, V.A.; Yang, Y.; Lee, B.J.; Flader, I.; Kenny, T.W. Mode-matching of wineglass mode disk resonator gyroscope in (100) single crystal silicon. *J. Microelectromech. Syst.* **2014**, *24*, 343–350. [[CrossRef](#)]
15. Ahn, C.H.; Nitzan, S.; Ng, E.J.; Hong, V.A.; Yang, Y.; Kimbrell, T.; Horsley, D.A.; Kenny, T.W. Encapsulated high frequency (235 kHz), high-Q (100 k) disk resonator gyroscope with electrostatic parametric pump. *Appl. Phys. Lett.* **2014**, *105*, 243504. [[CrossRef](#)]
16. Darvishian, A.; Shiari, B.; Cho, J.Y.; Nagourney, T.; Najafi, K. Anchor loss in hemispherical shell resonators. *J. Microelectromech. Syst.* **2017**, *26*, 51–66. [[CrossRef](#)]
17. Shao, P.; Mayberry, C.L.; Gao, X.; Tavassoli, V.; Ayazi, F. A polysilicon microhemispherical resonating gyroscope. *J. Microelectromech. Syst.* **2014**, *23*, 762–764. [[CrossRef](#)]
18. Senkal, D.; Ahamed, M.J.; Trusov, A.A.; Shkel, A.M. Achieving sub-Hz frequency symmetry in micro-glassblown wineglass resonators. *J. Microelectromech. Syst.* **2013**, *23*, 30–38. [[CrossRef](#)]
19. Sharma, A.; Zaman, M.F.; Ayazi, F. A Sub-0.2°/hr Bias Drift Micromechanical Silicon Gyroscope With Automatic CMOS Mode-Matching. *IEEE J. Solid-State Circuits* **2009**, *44*, 1593–1608. [[CrossRef](#)]
20. Su, J.; Xiao, D.; Wu, X.; Hou, Z.; Chen, Z. Improvement of bias stability for a micromachined gyroscope based on dynamic electrical balancing of coupling stiffness. *J. Micro. Nanolithogr. MEMS MOEMS* **2013**, *12*, 033008. [[CrossRef](#)]
21. Hou, Z.; Wu, X.; Xiao, D.; Chen, Z.; Su, J. Transition interface for improving the temperature characteristics of micromachined gyroscopes. *Microsyst. Technol.* **2014**, *20*, 227–234. [[CrossRef](#)]
22. Xiao, D.; Wang, X.; Zhou, Z.; Wu, X.; Chen, Z.; Hou, Z. A novel fabrication method based on an after thermal oxidation process for the realization of silicon-beams with normative polygon cross sections shapes. *Microsyst. Technol.* **2013**, *19*, 1081–1086. [[CrossRef](#)]
23. Xiao, D.; Cao, S.; Hou, Z.; Chen, Z.; Wang, X.; Wu, X. Enhanced sensitivity in a butterfly gyroscope with a hexagonal oblique beam. *AIP Adv.* **2015**, *5*, 041331. [[CrossRef](#)]



24. Andersson, G.; Hedenstierna, N.; Svensson, P. A Novel Silicon Bulk Gyroscope. *J. Ext. Abstr. Transducers* **1999**, *1*, 902–905.
25. Hedenstierna, N.; Habibi, S.; Nilsen, S.M.; Kvisteroy, T.; Jensen, G.U. Bulk micromachined angular rate sensor based on the 'butterfly'-gyro structure. In *Technical Digest, Proceedings of the 14th IEEE International Conference on Micro Electro Mechanical Systems (MEMS 2001), Interlaken, Switzerland, 25 January 2001*; IEEE: Piscataway, NJ, USA, 2001; pp. 178–181.
26. Andersson, G.; Hedenstierna, N.; Svensson, P. An Arrangement for Measuring Angular Velocity. U.S. Patent 6467349B1, 22 October 1998.
27. Ou, F.; Hou, Z.; Wu, X.; Xiao, D. Analysis and Design of a Polygonal Oblique Beam for the Butterfly Vibratory Gyroscope with Improved Robustness to Fabrication Imperfections. *Micromachines* **2018**, *9*, 198. [[CrossRef](#)]
28. Hibbeler, R.C. *Mechanics of Materials*; Publishing House of Electronic Industry: Beijing, China, 2004.
29. Xiao, D.; Su, J.; Chen, Z.; Hou, Z.; Wang, X.; Wu, X. Improvement of mechanical performance for vibratory microgyroscope based on sense mode closed-loop control. *J. Micro. Nanolithogr. MEMS MOEMS* **2013**, *12*, 023001. [[CrossRef](#)]
30. Xiao, D.; Xie, L.; Hou, Z.; Wu, X.; Li, S. Analyzing the frequency response of micromachined capacitive inertial devices by the third harmonic detection. In *Proceedings of the 2009 4th IEEE International Conference on Nano/Micro Engineered and Molecular Systems, Shenzhen, China, 5–8 January 2009*; pp. 339–342.
31. Leland, R. Mechanical Thermal Noise in Vibrational Gyroscopes. *IEEE Sens. J.* **2005**, *5*, 493–500. [[CrossRef](#)]



© 2019 by the authors. Licensee MDPI, Basel, Switzerland. This article is an open access article distributed under the terms and conditions of the Creative Commons Attribution (CC BY) license (<http://creativecommons.org/licenses/by/4.0/>).